Cancer Therapeutics

DOI: 10.1002/anie.201405490

A Multifunctional Nanomicelle for Real-Time Targeted Imaging and Precise Near-Infrared Cancer Therapy**

Jiangwei Tian, Lin Ding, Huangxian Ju, Yongchao Yang, Xilan Li, Zhen Shen, Zhi Zhu, Jun-Sheng Yu,* and Chaoyong James Yang**

Abstract: *Simultaneous targeted cancer imaging, therapy and real-time therapeutic monitoring can prevent over- or under-treatment. This work describes the design of a multifunctional nanomicelle for recognition and precise near-infrared (NIR) cancer therapy. The nanomicelle encapsulates a new pH-activatable fluorescent probe and a robust NIR photosensitizer, R16FP, and is functionalized with a newly screened cancer-specific aptamer for targeting viable cancer cells. The fluorescent probe can light up the lysosomes for real-time imaging. Upon NIR irradiation, R16FP-mediated generation of reactive oxygen species causes lysosomal destruction and subsequently trigger lysosomal cell death. Meanwhile the fluorescent probe can reflect the cellular status and in situ visualize the treatment process. This protocol can provide molecular information for precise therapy and therapeutic monitoring.*

Despite rapid advances in diagnostic and therapeutic procedures, cancer remains one of the most deadly diseases in the world today.[1] There is a strong need to identify new targets and develop novel approaches for accurate cancer detection and targeted therapy. Recently, the lysosome has been identified as a promising diagnostic and pharmacological target for effective cancer treatment.[2] It is distinct from other cellular organelles due to its weak acidic environment (pH 4.5–5.0) relative to the cytoplasm (pH 7.2).[3,4] The pH gradients are maintained by pumping protons from the cytosol across lysosomal membrane via vacuolar-type H^+-ATPase.[5] The unique pH characteristic endows the possibility for lysosome-targeted and pH-activatable cell imaging[6] and the improvement of signal-to-background ratio (SBR).[7] More interestingly, lysosome is also regarded to be involved in cell death[8] through releasing lysosomal hydrolases such as cathepsins into cytosol.[9] This release occurs in a process of lysosome membrane permeabilization (LMP),[10] which can be induced by various stimuli, for example, reactive oxygen species (ROS) generated under irradiation in the presence of photosensitizer.[8a,b,11] Therefore, it can be reasonably speculated that lysosome can serve as a target for cancer imaging and therapy ex vivo and in vivo.

Although some lysosomal fluorescent probes[12] or lysosomotropic detergents[13] have been developed for cancer imaging or therapy, these agents lack specificity to distinguish the lysosomes of cancer cells from those of normal cells, resulting in false-positive fluorescence or unwanted damages to normal cells. Moreover, the reported imaging and therapy procedures are basically implemented separately, which leads to low therapeutic and economic efficiency. In particular, a challenge is the inability to in situ monitor the characteristic biochemical changes during the whole therapy, thus failing to timely obtain the therapeutic feedback for precise treatment.

Here we describe the screening a cancer-specific aptamer and its integration with a newly synthesized pH-activatable fluorescent probe BDP-688 and a novel photosensitizer R16FP to design a multifunctional nanomicelle (Apt-TNP) for selective recognition of cancer cells and lysosome-based cancer-specific imaging, near-infrared (NIR, 700–1000 nm) photodynamic therapy (PDT), and particularly self-feedback of therapeutic efficacy (Scheme 1). The R16FP-mediated NIR PDT is ideal for high tissue penetration. The self-feedback function resulted from the fast and reversible fluorescence response to pH, which enabled the real-time visualization of lysosomal pH gradient change and precise therapy. The strategy provided a powerful tool for real-time evaluating cancer treatments.

Aptamers are characterized by high affinity and specificity, smaller size than antibodies, ease of synthesis and modification, high stability and low immunogenesis.[14] To achieve target-cell-specific delivery, human breast cancer MDA-MB-231 and normal human mammary epithelial MCF-10A cells were chosen for selection of a specific aptamer. Through a cell-SELEX process,[14e] an aptamer named as Apt S1 (Scheme 1 b) with high affinity and excellent specificity was selected against MDA-MB-231 cells after a 15-round selection (Figure S1, S2 and Table S1 in the Supporting Information). Apt S1 could also efficiently bind to breast

---

[*] J. Tian,[+] Dr. L. Ding,[+] Prof. H. Ju, Dr. Y. Yang, Prof. Z. Shen, Prof. J.-S. Yu
State Key Laboratory of Analytical Chemistry for Life Science, State Key Laboratory of Coordination Chemistry, School of Chemistry and Chemical Engineering, Nanjing University
Nanjing 210093 (P.R. China)
E-mail: hxju@nju.edu.cn
jsyu@nju.edu.cn

X. Li, Dr. Z. Zhu, Prof. C. J. Yang
State Key Laboratory of Physical Chemistry of Solid Surface, Key Laboratory for Chemical Biology of Fujian Province, Key Laboratory of Analytical Sciences, College of Chemistry and Chemical Engineering, Xiamen University
Xiamen 361005 (P.R. China)
E-mail: cyyang@xmu.edu.cn

[+] These authors contributed equally to this work.

[**] This study was supported by the National Basic Research Program (2010CB732400), the National Science Fund for Creative Research Groups (21121091 and 21021062) and the National Natural Science Foundation of China (21322506, 21005037, 21135002, 91213301, 20875045).

Supporting information for this article is available on the WWW under http://dx.doi.org/10.1002/anie.201405490.

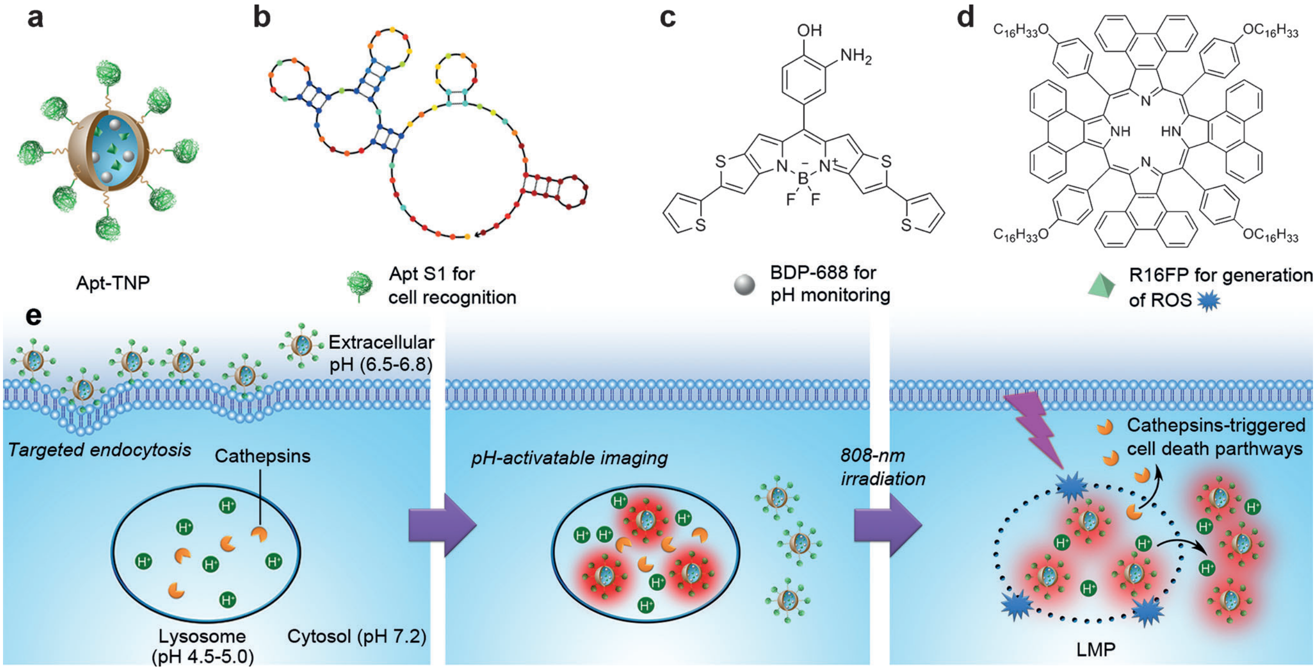

Scheme 1. Structures of a) Apt-TNP, b) Apt S1, c) BDP-688, and d) R16FP. e) Lysosome-aimed strategy for simultaneously targeted delivery, lysosomal imaging and destruction, and real-time self-feedback of therapeutic efficacy.

cancer tissues (Figure S3), but did not recognize normal tissues or cells or other cancer cells tested (Table S2).

For pH-activatable fluorescence imaging, BDP-688, a bithiophene-fused boron-dipyrromethene (BODIPY) fluorophore with a 2-aminophenol moiety at the *meso*-position (Scheme 1 c) was synthesized. The introduction of bithiophene into the BODIPY core led to red-shifted absorption and emission,[15] which could reduce the influence of autofluorescence in cell or tissue,[16] and the substitution of 2-aminophenol moiety contributed to the pH-sensitive fluorescence. BDP-688 displayed maximum absorbance at 660 nm with a molar absorption coefficient ε of $1.78\times10^5\,\text{M}^{-1}\,\text{cm}^{-1}$ (Figure S4). It was almost nonfluorescent in neutral pH solution, in which the fluorescence quantum yield Φ_{fl} was less than 0.003 due to the photoinduced electron transfer (PET) from the 2-aminophenol moiety to the excited fluorophore, and became highly fluorescent in acidic pH solution with Φ_{fl} of 0.45 at pH 5.0.

PDT combines a photosensitizer, light and molecular oxygen ($^3O_2$) to generate cytotoxic ROS, especially singlet oxygen ($^1O_2$), for cancer treatment. It displays fewer side effects than surgery, radiation therapy, and chemotherapy.[17] For in vivo use, the photosensitizer should be activated under NIR light for obtaining the maximum tissue penetration.[17b] According to these requirements, R16FP, a tetraphenanthroporphyrin-based photosensitizer with 4-(hexadecyloxy)-phenyl at *meso*-position (Scheme 1 d), was synthesized. This photosensitizer showed a broad NIR absorption band with maximum absorbance at 850 nm ($\varepsilon = 3.14\times10^4\,\text{M}^{-1}\,\text{cm}^{-1}$) (Figure S4). Upon excitation at 595 nm or 850 nm, R16FP displayed a NIR emission at 905 nm with Φ_{fl} of 7.4×10^{-3} (Figure S5). In the presence of oxygen the emission spectra showed a peak at 1275 nm, which demonstrated the efficient $^1O_2$ generation by R16FP, and could be further confirmed by monitoring the decrease of 410 nm absorbance with a $^1O_2$ indicator (Figure S6). From the absorbance and emission spectra of BDP-688 (Figure S4 and S7) and R16FP (Figure S4 and S5), no spectral overlap existed, thus their spectral interactions could be excluded.

The Apt-TNP could be prepared using poly(lactic acid)-*block*-poly (ethylene oxide) copolymer with a carboxy terminal group (PLA-PEG-COOH) as the nanomatrix. The transmission electron microscopic (TEM) image of Apt-TNP showed well-dispersed spherical-shaped nanoparticles (Figure S8) with a hydrodynamic diameter of 160.0 ± 12.7 nm (Figure S9). Upon covalent linkage of Apt S1 to the BDP-688 and R16FP-loaded nanomatrix, the zeta potential changed from −27.8 ± 2.4 to −38.9 ± 3.2 mV (Figure S10). The Apt-TNP exhibited good fluorescence stability in weakly acidic media in air (Figure S11). The standard fluorescence pH titration gave an apparent pK_a value of 5.7 for Apt-TNP (Figure S7), suggesting a sensitive pH response capability in the physiologically acidic pH range (4.5–6.9). Furthermore, the switchable fluorescence of Apt-TNP responded to pH change reversibly and instantly (Figure S12), thereby holding promise for feeding back the intracellular pH fluctuations during therapeutic process.

After incubating MDA-MB-231 cells with Apt-TNP for 2 h, some fluorescent spots were observed within the cells, and its intensity increased with increasing incubation time (Figure 1 a), indicating a gradual internalization of Apt-TNP into the acidic organelles. In contrast, MCF-10A cells did not show any fluorescent signal even after incubation with Apt-TNP for 16 h (Figure 1 a). The fluorescence intensity of Apt-TNP-loaded MDA-MB-231 cells exhibited a position-sensitive dependence (Figure 1 b,c). The co-staining experiment

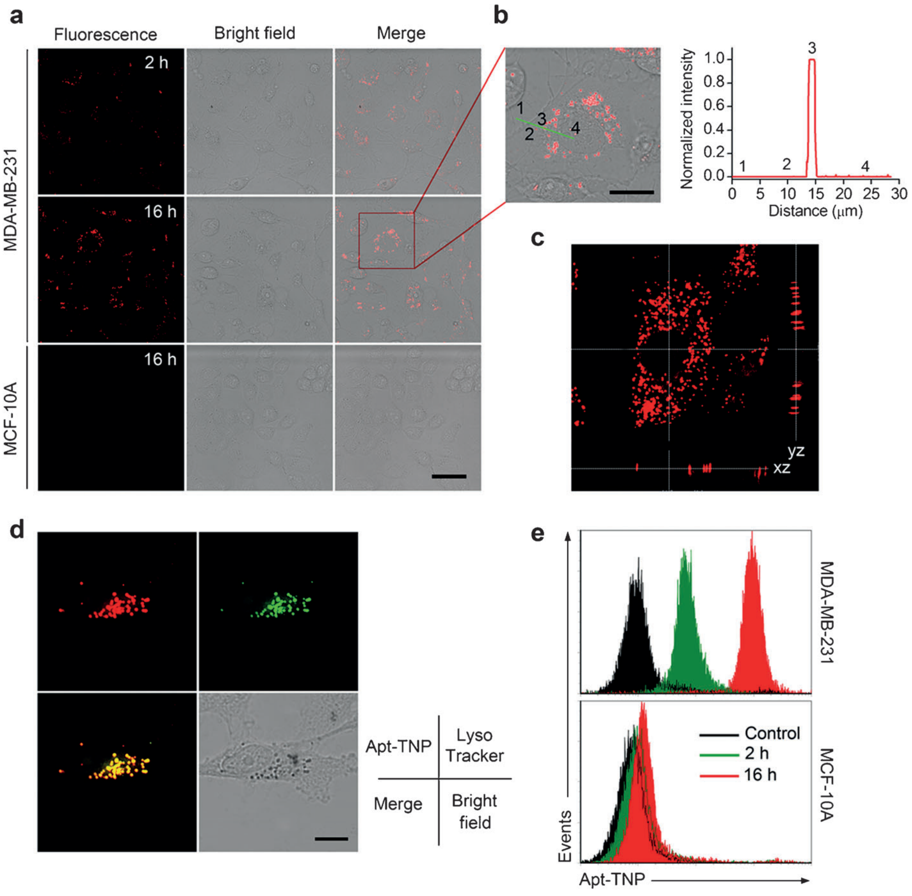

Figure 1. Targeted imaging of cancer cells with Apt-TNP. a) Confocal fluorescence images of living MDA-MB-231 and MCF-10A cells after incubation with Apt-TNP for 2 or 16 h at $\lambda_{ex/em}$ of 633/660–720 nm. Scale bar, 50 μm. b) Subcellular fluorescent intensity analysis of Apt-TNP-loaded MDA-MB-231 cells. Left: Amplified images shown in (a). Scale bar, 25 μm. Right: Fluorescence intensity profile across the line as shown in left image, which corresponds to extracellular region 1, cytosol 2, lysosome 3, and nuclear region 4. c) Stack image for Z-depth scanning of Apt-TNP-loaded MDA-MB-231 cells. d) Colocalization images of MDA-MB-231 cells co-incubated with Apt-TNP and LysoTracker Green. Scale bar, 10 μm. e) Flow cytometric assay of MDA-MB-231 and MCF-10A cells incubated with Apt-TNP for 2 and 16 h.

with LysoTracker Green, a lysosomal indicator, showed that the localization of Apt-TNP fluorescence was in the lysosomal compartment (Figure 1 d), which demonstrated that the acidic pH activatable fluorescence of Apt-TNP was in lysosomes. Although lysosomes also exist in normal MCF-10A cells, the selective recognition of Apt S1 on the Apt-TNP surface to MDA-MB-231 cells (Figure S13) led to the targeted imaging of cancer cell lysosomes. Flow cytometric analysis further demonstrated the specific imaging capability of Apt-TNP for cancer cells (Figure 1 e).

The targeted PDT capability of Apt-TNP on the cancer cells was verified with NIR irradiation at 808 nm. After incubation with Apt-TNP, the irradiation induced MDA-MB-231 cells swelling and the rupture of the outer membrane (Figure S14a), indicating obvious cell death. In contrast, no obvious morphologic change was observed for Apt-TNP-incubated MCF-10A cells before and after irradiation. Thus, the Apt-TNP-mediated PDT killed only cancer cells, as further confirmed by Annexin V-FITC Apoptosis Assay using flow cytometry (Figure S14b). After 120 J cm^{-2} irradiation, the percentage of dead cells in Apt-TNP-loaded MDA-MB-231 group increased from 5.68 % to 89.63 %, while the percentage of dead cells in the absence of Apt-TNP showed only a slight change from 5.16 % to 7.15 %. The MCF-10A cells were insensitive to the irradiation or the Apt-TNP with dead cell percentages in the range of 8.40 % to 9.14 %. These results confirmed the capability of Apt-TNP for targeted PDT against the corresponding cancer cells.

The cell death induced by Apt-TNP-mediated PDT was further demonstrated by trypan blue dye exclusion assay (Figure S15), colony formation assay (Figure S16), MTT assay (Figure S17), and TUNEL assay (Figure S18). In the presence of both Apt-TNP and irradiation, MDA-MB-231 cells showed high death rates, while the absence of either Apt-TNP or irradiation resulted in negligible changes in the cells. Furthermore, the cell death rate was found to be irradiation dose-dependent (Figure S15 and S16) and Apt-TNP concentration-dependent (Figure S17). To probe the cell death mechanism during the Apt-TNP-mediated PDT, 2′,7′-dichlorfluorescein-diacetate (DCFH-DA) was used as a ROS probe, vitamin C as a ROS scavenger and antipain as a cathepsin inhibitor in the culture medium, respectively. After incubation of cancer cells with Apt-TNP and DCFH-DA, the fluorescence from the specific oxidation product of DCFH-DA by ROS as dichlorofluorescein (DCF) could be observed in the cells upon irradiation. The DCF fluorescence intensity increased with the growing irradiation dose (Figure S19), indicating the irradiation dose-dependent generation of ROS. Moreover, the presence of vitamin C in the cells led to effective inhibition of cell death (Figure S20a), suggesting that ROS played important roles in the killing process. Because the ROS could destroy the lysosomes and induce the release of cathepsins to cytosol,[9] the contribution of cathepsins to cell death was also investigated with an antipain inhibition experiment. With the increasing antipain concentration, the percentage of cell death decreased significantly (Figure S20b), confirming that the cell death was associated with the released cathepsins. Taking together, the possible cell death mechanism can be reasonably speculated as that Apt-TNP-mediated PDT damages the lysosomes of cancer cells by the generated ROS and results in a cathepsin-related cell death pathways.

The unique pH-responsive fluorescence of Apt-TNP made it possible to monitor the cellular pH change in situ and real-time, which contributed to the self-feedback of therapeutic response during PDT and investigation of lysosomal cell-death pathways. To verify this capability, the fluorescent and morphologic changes of Apt-TNP-loaded MDA-MB-231 cells under 808 nm irradiation were tracked in real-time by confocal fluorescence imaging (Video S1). As predicted, at the beginning of PDT, bright fluorescence was observed in the lysosomes (Figure 2a), showing well maintained pH gradients and good cell viability. Upon irradiation, while the morphology changes were not significant, the lysosomal fluorescence gradually decreased, and the cytoplasm fluorescence became brighter during the first 8 min (Figure 2b–d), suggesting that the generated ROS caused LMP and proton release from the lysosomes to the cytosol. After 8 min irradiation, more and more bubbles appeared on the surface of cells and the fluorescence in the lysosomes and cytoplasm gradually decreased (Figure 2e–h). After 20 min irradiation, the outer membrane was ruptured and no fluorescence signal could be observed, indicating the obvious cell death. By collecting the fluorescence signals in the lysosome and cytoplasm (Figure 2i), the gradually decreasing fluorescence in lysosome and the fluorescence change in cytosol could be observed (Figure 2j), which demonstrated the gradual decrease in cytoplasmic pH due to LMP during the first 8 min, followed by a pH rise as the cell membrane ruptured. The fluorescent and morphologic changes of Apt-TNP-loaded MDA-MB-231 cells in the absence of 808 nm irradiation (Video S2 and Figure S21) or Apt-TNP (without R16FP encapsulation)-loaded cells under 808 nm irradiation (Video S3 and Figure S22) were also monitored in real-time. In the absence of either irradiation or photosensitizer, two necessary elements for generating ROS to induce cell death, no fluorescence change was observed. These results indicated that the real-time self-feedback of intracellular pH change by Apt-TNP provided a reliable and convenient method for therapeutic monitoring and an efficient protocol for the visualization of lysosomal cell-death pathways.

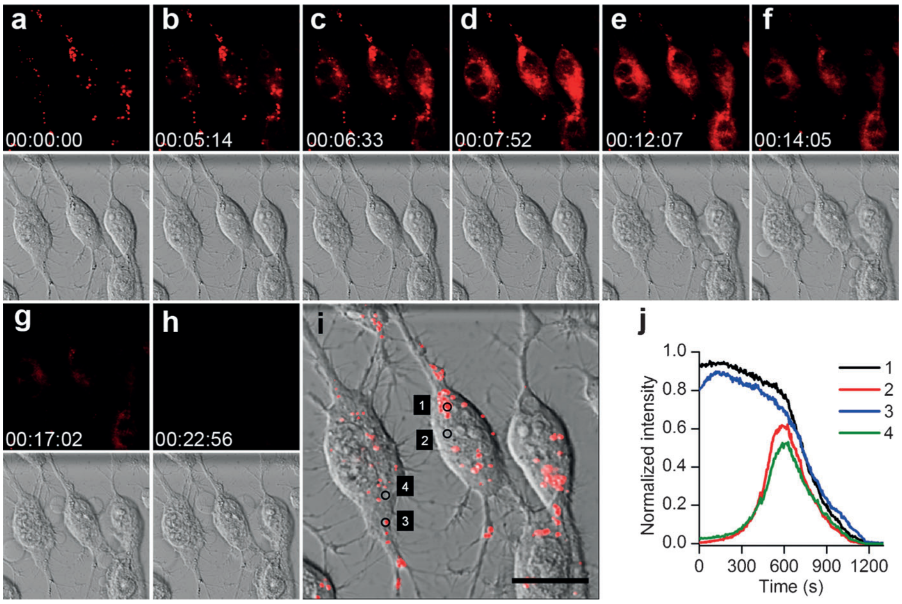

Figure 2. Real-time monitoring of fluorescence and morphology during PDT. a–h) Real-time fluorescence images at $\lambda_{ex/em}$ of 633/660–720 nm (top) and bright-field images (bottom) of Apt-TNP-loaded MDA-MB-231 cells under 808 nm irradiation at a power of 100 mW cm^{-2}. i) Merged fluorescence and bright field image at the starting time of PDT. Scale bar, 20 μm. j) Time course of fluorescence intensity collected at dots 1–4 shown in (i), corresponding to the lysosomes (1, 3) and cytosol (2, 4).

The blood circulation curve of the Apt-TNP in mice showed the biphasic clearance profile with a rapid clearance during the first 6 h followed by a continuous and slow elimination rate (Figure S23). The blood circulation half-life was found to be 5.2 h, which indicated a long persistence of Apt-TNP in bloodstream to corroborate the stability in vivo.[11]

The feasibility of in vivo targeted cancer imaging with Apt-TNP was investigated in subcutaneous or orthotopic MDA-MB-231 tumor-bearing BALB/c nude mice. After intravenous (i.v.) injection of Apt-TNP into the subcutaneous MDA-MB-231 tumor-bearing mice, the cancer site could be distinguished from the surrounding normal tissue at 6 h postinjection (p.i.). The SBR increased gradually and reached a maximum at 24 h p.i., which was maintained even after 48 h p.i. (Figure 3a), demonstrating the targeted delivery and long retention of Apt-TNP in cancer tissue. Moreover, compared with the fluorescence of Apt-TNP in cancer tissue, the fluorescence in other regions of the mouse body was negligible (Figure 3b). The evaluation of excised tissues showed that the strongest fluorescence occurred in the cancer tissue, while the liver and kidneys showed weak fluorescence (Figure 3c), which provided further evidence for the targeted imaging of cancer tissue, and suggested that Apt-TNP could be eliminated in hepatobiliary and renal excretion pathways from the body.[6b] Considering the similarity of the biological environment in the orthotopic cancer model to human cancer tissue, the utility of Apt-TNP for imaging orthotopic cancer was examined. After i.v. injection of TNP (without Apt), Random DNA-TNP and Apt-TNP for 24 h, the Apt-TNP-administrated mice displayed the highest specific contrast for cancer imaging (Figure 3d). Overall, the contribution of Apt S1 to targeting and the fluorescence sensitivity of BDP-688 to acidic pH resulted in successful in vivo cancer imaging by Apt-TNP with high SBR.

The efficacy of Apt-TNP-mediated PDT was assessed by monitoring the tumor volume and H&E staining of tumor tissue after treatment. No therapeutic effect or tumor tissue necrosis was observed in control groups of tumor-bearing

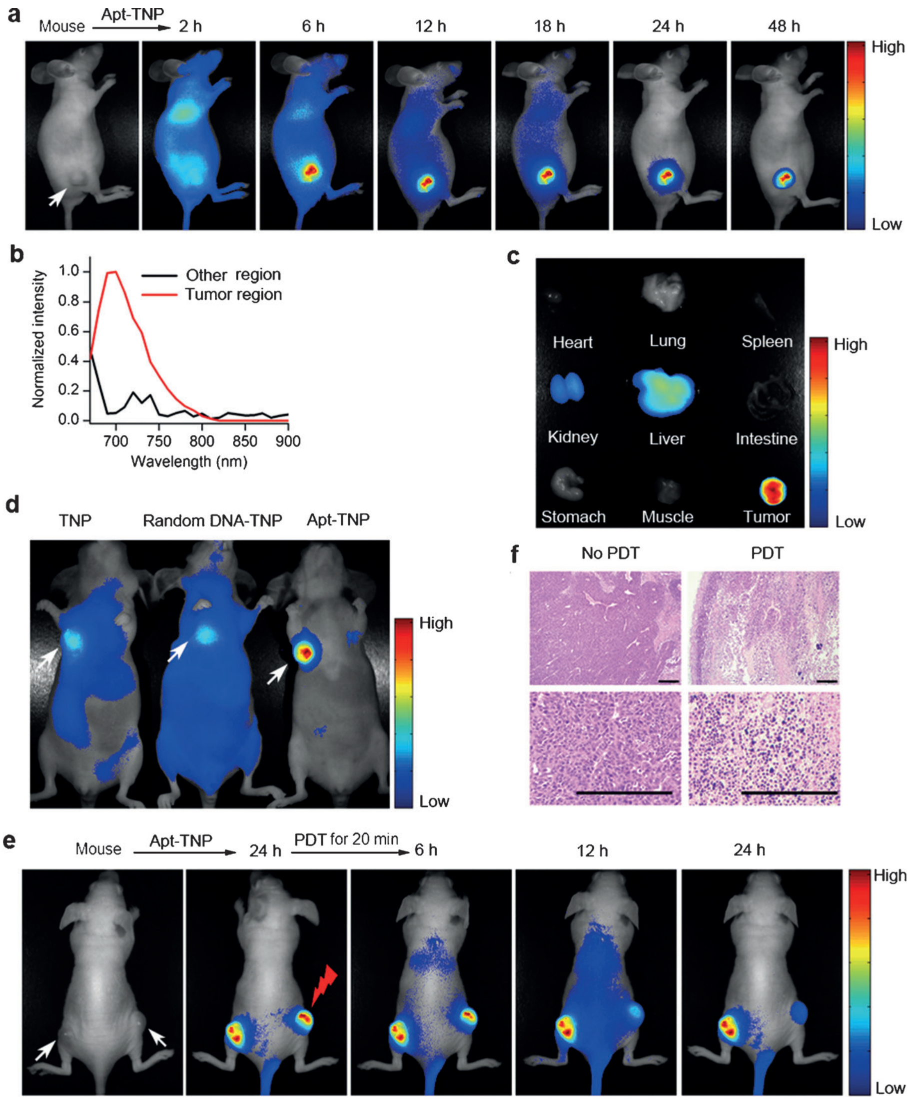

Figure 3. In vivo targeted cancer imaging, PDT and therapeutic monitoring with Apt-TNP. The arrows show the cancer sites. a) Time-dependent in vivo fluorescence images of subcutaneous MDA-MB-231 tumor-bearing mice after i.v. injection of Apt-TNP. b) In vivo fluorescence spectra of MDA-MB-231 tumor-bearing mice at cancer tissue and other region. c) Ex vivo fluorescence biodistribution image of organs and cancer tissue from MDA-MB-231 tumor-bearing mice sacrificed at 24 h p.i. of Apt-TNP. d) In vivo fluorescence image of orthotopic MDA-MB-231 tumor-bearing mice at 24 h p.i. of TNP (without Apt), Random DNA-TNP and Apt-TNP. e) In vivo PDT and therapeutic monitoring on subcutaneous MDA-MB-231 tumor-bearing mice with Apt-TNP. After 24 h p.i., the right tumor was irradiated with 808 nm laser, the left tumor was kept in dark as control. f) H&E staining of the left and right MDA-MB-231 tumor tissues followed with no PDT and PDT. Scale bars, 200 μm.

mice treated with Apt-TNP or 808 nm irradiation alone (Figure S24), revealing that Apt-TNP had little dark toxicity and the irradiation had no photothermal effect due to the low power density of 100 mW cm^{-2} compared with previously used 2–4 W cm^{-2}.[18] After the tumor-bearing mice were treated with Apt-TNP + irradiation, tumor growth could be significantly inhibited and the tumor tissue showed obvious necrosis (Figure S24), indicating the high PDT efficacy of Apt-TNP. Notably, the H&E-stained organ slices from the PDT-treated mice did not show obvious sign of organ damage (Figure S25), suggesting the negligible toxic side effects of Apt-TNP for in vivo applications. Furthermore, mice bearing two MDA-MB-231 tumors (one on each flank) were intravenously injected with Apt-TNP to perform PDT and monitor the therapeutic efficacy with Apt-TNP. At 24 h p.i., both MDA-MB-231 tumors were selectively visualized with high SBR (Figure 3e). Afterward, only the right tumor was irradiated with an 808 nm laser at 100 mW cm^{-2} for 20 min. The fluorescence intensity from the irradiated tumor gradually decreased and almost disappeared after 24 h. In contrast, there was negligible change in fluorescence observed for the unirradiated tumor. In order to investigate the physiological transformation along with the fluorescent change after PDT, H&E staining of the two tumors was performed. Prominent necrosis was observed in the PDT-treated cancer tissue, while necrosis was indiscernible in the unirradiated tumor (Figure 3 f). From the results above, it is reasonable to conclude that Apt-TNP displays not only an effective therapy function but also a self-feedback capability for monitoring the therapeutic efficacy.

In summary, by integrating the newly screened Apt S1 and designed BDP-688 and R16FP with PLA-PEG-COOH, we propose a multifunctional Apt-TNP for simultaneous cancer imaging with high SBR, efficient 808 nm-irradiated PDT and real-time therapeutic monitoring. With the specific pH-activatable fluorescence guiding, the PDT can be accurately performed on diseased tissue. The PDT-induced cancer cell death is attributed to the generated ROS by Apt-TNP under irradiation. The ROS cause LMP and subsequent cathepsins release to trigger cell death-pathways. The subtle pH change at subcellular level during the cell-death process has been visualized by monitoring the pH-activatable fluorescence of Apt-TNP, providing a valuable and convenient self-feedback function for PDT efficacy tracking. We believe that the proposed Apt-TNP offers a new paradigm for precise cancer therapy and contributes to the acquirement of deep insight into the complex molecular mechanisms of lysosome-related life processes.

Received: May 21, 2014

Keywords: cancer · fluorescence imaging · lysosome · photodynamic therapy · therapeutic monitoring

[1] R. Siegel, D. Naishadham, A. Jemal, *CA-Cancer J. Clin.* **2013**, *63*, 11 – 30.

[2] a) Y. H. Hung, L. M. Chen, J. Y. Yang, W. Y. Yang, *Nat. Commun.* **2013**, *4*, 2111; b) N. H. Petersen, O. D. Olsen, L. Groth-Pedersen, A. M. Ellegaard, M. Bilgin, S. Redmer, M. S. Ostenfeld, D. Ulanet, T. H. Dovmark, A. Lønborg, S. D. Vindeløv, D. Hanahan, C. Arenz, C. S. Ejsing, T. Kirkegaard, M. Rohde, J. Nylandsted, M. Jäättelä, *Cancer Cell* **2013**, *24*, 379 – 393.

[3] J. P. Luzio, P. R. Pryor, N. A. Bright, *Nat. Rev. Mol. Cell Biol.* **2007**, *8*, 622 – 632.

[4] J. R. Casey, S. Grinstein, J. Orlowski, *Nat. Rev. Mol. Cell Biol.* **2010**, *11*, 50 – 61.

[5] J. A. Mindell, *Annu. Rev. Physiol.* **2012**, *74*, 69 – 86.

[6] a) Y. Urano, D. Asanuma, Y. Hama, Y. Koyama, T. Barrett, M. Kamiya, T. Nagano, T. Watanabe, A. Hasegawa, P. L. Choyke, H. Kobayashi, *Nat. Med.* **2009**, *15*, 104 – 109; b) H. Lee, W. Akers, K. Bhushan, S. Bloch, G. Sudlow, R. Tang, S. Achilefu, *Bioconjugate Chem.* **2011**, *22*, 777 – 784; c) K. Zhou, Y. Wang, X. Huang, K. Luby-Phelps, B. D. Sumer, J. Gao, *Angew. Chem.* **2011**, *123*, 6233 – 6238; *Angew. Chem. Int. Ed.* **2011**, *50*, 6109 – 6114; d) Y. Wang, K. Zhou, G. Huang, C. Hensley, X. Huang, X. Ma, T. Zhao, B. D. Sumer, R. J. DeBerardinis, J. Gao, *Nat. Mater.* **2014**, *13*, 204 – 212.

[7] H. Kobayashi, P. L. Choyke, *Acc. Chem. Res.* **2011**, *44*, 83 – 90.

[8] a) M. E. Guicciardi, M. Leist, G. J. Gores, *Oncogene* **2004**, *23*, 2881 – 2890; b) G. Kroemer, M. Jäättelä, *Nat. Rev. Cancer* **2005**, *5*, 886 – 897; c) T. Yamashima, S. Oikawa, *Prog. Neurobiol.* **2009**, *89*, 343 – 358.

[9] a) C. E. Chwieralski, T. Welte, F. Bühling, *Apoptosis* **2006**, *11*, 143 – 149; b) S. Conus, H. U. Simon, *Biochem. Pharmacol.* **2008**, *76*, 1374 – 1382; c) U. Repnik, V. Stoka, V. Turk, B. Turk, *Biochim. Biophys. Acta Proteins Proteomics* **2012**, *1824*, 22 – 33.

[10] P. Boya, G. Kroemer, *Oncogene* **2008**, *27*, 6434 – 6451.

[11] J. Tian, L. Ding, H. J. Xu, Z. Shen, H. Ju, L. Jia, L. Bao, J. S. Yu, *J. Am. Chem. Soc.* **2013**, *135*, 18850 – 18858.

[12] a) F. Rashid, R. W. Horobin, M. A. Williams, *Histochem. J.* **1991**, *23*, 450 – 459; b) X. Wang, D. M. Nguyen, C. O. Yanez, L. Rodriguez, H. Y. Ahn, M. V. Bondar, K. D. Belfield, *J. Am. Chem. Soc.* **2010**, *132*, 12237 – 12239; c) L. Wang, Y. Xiao, W. Tian, L. Deng, *J. Am. Chem. Soc.* **2013**, *135*, 2903 – 2906.

[13] a) D. K. Miller, E. Griffiths, J. Lenard, R. A. Firestone, *J. Cell Biol.* **1983**, *97*, 1841 – 1851; b) W. Li, X. Yuan, G. Nordgren, H. Dalen, G. M. Dubowchik, R. A. Firestone, U. T. Brunk, *FEBS Lett.* **2000**, *470*, 35 – 39.

[14] a) J. Gao, X. Gao, L. Su, H. Xia, G. Gu, Z. Pang, X. Jiang, L. Yao, J. Chen, H. Chen, *Biomaterials* **2011**, *32*, 8010 – 8020; b) D. Shangguan, Y. Li, Z. Tang, Z. C. Cao, H. W. Chen, P. Mallikaratchy, K. Sefah, C. J. Yang, W. Tan, *Proc. Natl. Acad. Sci. USA* **2006**, *103*, 11838 – 11843; c) M. C. Estévez, Y. F. Huang, H. Kang, M. B. O'Donoghue, S. Bamrungsap, J. Yan, X. Chen, W. Tan, *Methods Mol. Biol.* **2010**, *624*, 235 – 248; d) Y. Wu, K. Sefah, H. Liu, R. Wang, W. Tan, *Proc. Natl. Acad. Sci. USA* **2010**, *107*, 5 – 10; e) X. Li, W. Zhang, L. Liu, Z. Zhu, G. Ouyang, Y. An, C. Zhao, C. J. Yang, *Anal. Chem.* **2014**, *86*, 6596 – 6603.

[15] Y. Yang, Q. Guo, H. Chen, Z. Zhou, Z. Guo, Z. Shen, *Chem. Commun.* **2013**, *49*, 3940 – 3942.

[16] a) V. Ntziachristos, C. Bremer, R. Weissleder, *Eur. Radiol.* **2003**, *13*, 195 – 208; b) A. Zaheer, R. E. Lenkinski, A. Mahmood, A. G. Jones, L. C. Cantley, J. V. Frangioni, *Nat. Biotechnol.* **2001**, *19*, 1148 – 1154.

[17] a) D. E. J. G. J. Dolmans, D. Fukumura, R. K. Jain, *Nat. Rev. Cancer* **2003**, *3*, 380 – 387; b) M. Ethirajan, Y. Chen, P. Joshi, R. K. Pandey, *Chem. Soc. Rev.* **2011**, *40*, 340 – 362; c) M. Mitsunaga, M. Ogawa, N. Kosaka, L. T. Rosenblum, P. L. Choyke, H. Kobayashi, *Nat. Med.* **2011**, *17*, 1685 – 1691; d) S. Cui, D. Yin, Y. Chen, Y. Di, H. Chen, Y. Ma, S. Achilefu, Y. Gu, *ACS Nano* **2013**, *7*, 676 – 688.

[18] a) G. von Maltzahn, J. H. Park, A. Agrawal, N. K. Bandaru, S. K. Das, M. J. Sailor, S. N. Bhatia, *Cancer Res.* **2009**, *69*, 3892 – 3900; b) K. Yang, S. Zhang, G. Zhang, X. Sun, S. T. Lee, Z. Liu, *Nano Lett.* **2010**, *10*, 3318 – 3323.